

Incipient quantum spin Hall insulator under strong correlations

Peizhi Mai¹, Jinchao Zhao¹, Philip W. Phillips^{1,†}

¹*Department of Physics and Institute of Condensed Matter Theory,
University of Illinois at Urbana-Champaign, Urbana, IL 61801, USA*

(Dated: today)

To assess prior mean-field studies that the interacting Kane-Mele model supports a novel antiferromagnetic Chern insulating phase (AFCI) for a wide range of sublattice potentials, we analyze the Kane-Mele-Hubbard model in the presence of a sublattice potential using determinant quantum Monte Carlo (DQMC). Instead of an AFCI, we find that the ground state is a quantum spin Hall (QSH) insulator for intermediate values of the sublattice potential λ_v , albeit with a small gap. The QSH state gives way to a trivial band insulator as the sublattice potential increases beyond a critical value. Only at small sublattice potentials does the QSH state transition into a trivial Mott insulator with xy antiferromagnetic correlations. The QAH feature is only observed at high temperature. The QAH feature crosses over to an incipient QSH state when the topological gap stabilizes. Our work is consistent with the experimental observation that in twisted bilayer MoTe₂[1–3] and WSe₂[4] as well as AB stacked MoTe₂/WSe₂[5, 6], where QSH is consistently observed at even-integer filling over a wide range of parameters.

INTRODUCTION

Two-dimensional (2D) moiré van der Waals materials continue to surprise us with discoveries such as the coexistence of the quantum anomalous Hall (QAH) and quantum spin Hall (QSH) in the same sample[5] and more recently fractional quantum anomalous Hall (FQAH) effects in twisted bilayer MoTe₂[1–3, 7] and rhombohedral graphene-hBN moiré systems[8]. These materials feature topological flat bands with high tunability, providing an ideal platform to study the interplay between strong correlations and topology. Thus far, the FQAH states observed at $\nu < 1$ are abelian. The analogy between FQAH and fractional quantum Hall effects (FQHE) has sparked a search for non-abelian anyons at higher fillings inspired by the $\nu = 5/2$ state in FQHE[9], which is crucial for topological quantum computation[10]. The recently discovered correlated QSH state at $\nu = 3$ in 2.1° twisted bilayer MoTe₂[11] emerges as a possible candidate for hosting non-abelian anyons. However, the nature of this QSH state remains under debate, particularly given the spontaneous ferromagnetism observed at the same filling in 2.6° twisted bilayer MoTe₂[12]. Despite this, it is closely related to the single, double, and triple QSH effects[11, 12] observed at $\nu = 2, 4, \text{ and } 6$, respectively. Understanding the influence of strong correlations on QSH system is crucial for characterizing the peculiar fractional states in higher Chern bands.

Twisted MoTe₂[1–3, 7, 11, 13] and WSe₂[4] as well as moiré heterobilayer transition metal dichalcogenides (TMD)[5] mimic the Kane-Mele (KM) physics under strong correlations. While studies on the Kane-Mele-Hubbard (KMH) model with various methods[14–17] consistently reveal a transition from a QSH insulator to a trivial Mott insulator (TriMI) with easy plane xy -antiferromagnetism (AFM _{xy}) at half-filling (corresponding to $\nu = 2$ in experiment) when the Hubbard U increases, the moiré TMD systems display QSH effects at even-integer fillings in a range of displacement fields[4, 5, 11]. This suggests that the presence of a displacement field may help sustain nontrivial topology against

strong correlations. Recent theoretical studies on the KMH model[18, 19], incorporating a sub-lattice potential λ_v (corresponding to the displacement field in experiment) have identified a QAH region with z -axis anti-ferromagnetism (AFM _{z}) at half-filling when both U and λ_v are large—referred to as the antiferromagnetic Chern insulator (AFCI). However, these studies primarily rely on *mean-field* theory (MFT). MFT may be useful after the symmetry is known to be broken and is nevertheless prone to exploring symmetry-breaking states in strongly correlated systems. Thus, exact methods are essential for investigating the true nature of possible symmetry breaking and the emergence of topological phases in these correlated systems.

In this study, we first demonstrate our method for distinguishing the topologies of QSH, QAH/AFCI, and trivial insulators using Streda’s formula applied to the non-interacting KM model with a sub-lattice potential λ_v and a symmetry-breaking AFM _{z} Zeeman field. This approach aligns with techniques used in recent experiments on twisted TMD systems[2–4]. We then turn off the AFM _{z} field and solve the KMH model at finite temperatures using the numerically exact determinant quantum Monte Carlo (DQMC) method. We observe that for large U and λ_v , the system exhibits a QAH feature at high temperatures. However, at sufficiently low temperature, an incipient QSH insulator emerges with a small gap. This contrasts with earlier MFT studies[18, 19], which predicted the stabilization of an AFCI state. Our results show that the AFM _{z} spin correlation is nearly temperature-independent and only slightly exceeds the AFM _{xy} spin correlation for large λ_v . Given the strong fluctuations, we conclude that AFM _{z} is unlikely to stabilize at finite temperatures, thereby preserving the QSH topology. As λ_v increases, the incipient QSH insulator transitions to a band insulator (BI), with an extended quasi semi-metal region around the phase boundary. Conversely, decreasing λ_v drives the incipient QSH insulator to a trivial Mott insulator without closing the single-particle charge gap. Our study is consistent with the ubiquitous observation of QSH effects at even-integer fill-

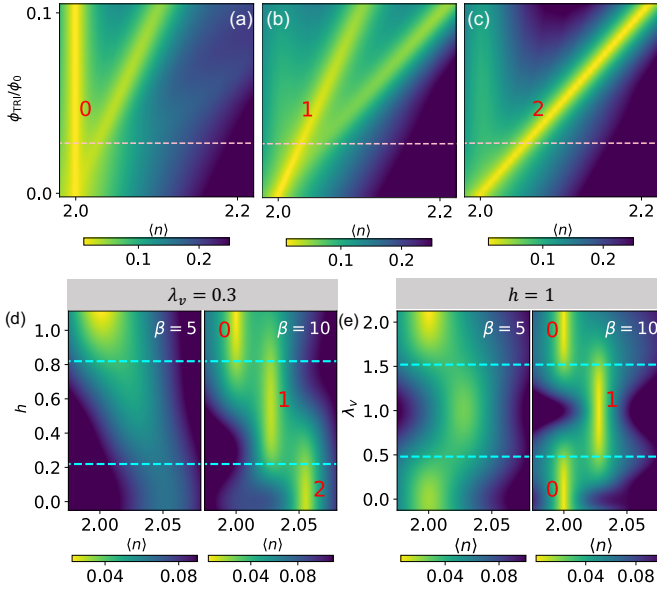


FIG. 1: Panels (a-c) show examples of TRI Compressibility χ_{TRI} as a function of density $\langle n \rangle$ and TRI magnetic flux ϕ_{TRI}/ϕ_0 for (a) trivial insulator ($C_s = 0$), (b) AFI ($C_s = 1$), (c) QSH insulator ($C_s = 2$). The inverse slope of the leading valley gives the spin Chern number labeled in red. The dashed line gives where we fix the flux $\phi_{\text{TRI}}/\phi_0 = 1/36$ for obtaining panels (d) and (e). Panel (d) show $\chi_{\text{TRI}}(\phi_{\text{TRI}}/\phi_0 = 1/36)$ as a function of $\langle n \rangle$ and h with $\lambda_v = 0.3$ at $\beta = 5$ and 10. The light regions show the dip and are associated with a spin Chern number as labeled in red. Panel (e) show $\chi_{\text{TRI}}(\phi_{\text{TRI}}/\phi_0 = 1/36)$ as a function of $\langle n \rangle$ and λ_v with $h = 1$ at $\beta = 5$ and 10. The dashed line in panels (d) and (e) depicts the phase boundary. All panels share the parameters $t' = 0.1$.

ing of twisted TMD systems in the presence of strong correlations.

MODEL

We consider the generalized KM model with a sub-lattice potential and an external magnetic field,

$$H_{\text{KM}} = t \sum_{\langle ij \rangle \sigma} e^{i\phi_{i,j}} c_{i\sigma}^\dagger c_{j\sigma} + t' \sum_{\langle\langle ij \rangle\rangle \sigma} e^{\pm i\psi\sigma} e^{i\phi_{i,j}} c_{i\sigma}^\dagger c_{j\sigma} - \mu \sum_{i,\sigma} n_{i\sigma} + \lambda_v \left(\sum_{i \in A, \sigma} n_{i\sigma} - \sum_{i \in B, \sigma} n_{i\sigma} \right), \quad (1)$$

where we set the nearest-neighbor hopping $t = 1$ as the energy scale in the honeycomb lattice. The next-nearest-neighbor hopping $t'e^{\pm i\psi\sigma}$ is the intrinsic spin-orbit coupling (SOC) with a generalized spin-dependent Haldane phase ψ [20]. We stick to $\psi = -\pi/2$ (the SOC in the original KM model) in this study unless otherwise specified. $\lambda_v \geq 0$ is the sub-lattice potential. The non-interacting half-filled system at zero magnetic flux is a QSH insulator given $\lambda_v < \lambda_v^c = |3\sqrt{3}t' \sin \psi|$. The effect of an external magnetic field is included through the standard Peierls substitution as the

phase factor $\exp(i\phi_{i,j})$, which is introduced to probe the zero-field topology[21, 22] and minimize finite-size effects[23] (see supplement). Here $\phi_{i,j} = (2\pi/\Phi_0) \int_{r_i}^{r_j} \mathbf{A} \cdot d\mathbf{l}$, where $\Phi_0 = e/h$ is the magnetic flux quantum, the vector potential $\mathbf{A} = (x\hat{y} - y\hat{x})B/2$ (symmetric gauge). The flux quantization condition $\Phi/\Phi_0 = n_f/N_c$ (with n_f an integer and N_c the number of unit cells) is fulfilled to ensure the single-valuedness of the wavefunction in a finite cluster. We also consider a time-reversal-invariant (TRI), namely spin-dependent, magnetic field $\phi_{\text{TRI}} = \sigma\phi$ for measuring the spin Chern number as illustrated below.

Let's first outline our approach to detect the relevant topological invariant, specifically the spin Chern number C_s and how an AFI can be induced by adding a symmetry-breaking AFM_z Zeeman field ($h \geq 0$) to the Hamiltonian Eq. (1):

$$H_{\text{KMAF}} = H_{\text{KM}} + h \left(\sum_{i \in A, \sigma} - \sum_{i \in B, \sigma} \right) (n_{i\uparrow} - n_{i\downarrow}). \quad (2)$$

The Zeeman field modifies the sub-lattice potential in a spin-dependent manner. For a small $\lambda_v < \lambda_v^c$ and $h < \lambda_v^c - \lambda_v$, the system remains in a QSH phase. As h increases within the range $\lambda_v^c - \lambda_v < h < \lambda_v^c + \lambda_v$, the system transitions into an intermediate AFI phase where one spin stays QAH while the other becomes trivial. If h continues to increase beyond $\lambda_v^c + \lambda_v$, the topology for both spins is destroyed. The spin Chern number $C_s = C_\uparrow - C_\downarrow$ is suitable to distinguish these three phases: QSH with $C_s = 2$, AFI with $C_s = 1$ and trivial insulator (TriI) with $C_s = 0$. This quantity can be measured by employing the streda formula in a system under TRI magnetic flux. The procedure involves plotting the compressibility as a function of flux ϕ_{TRI}/ϕ_0 (y-axis) and density $\langle n \rangle$ (x-axis) to locate the dominant valley (dips representing insulating states), as illustrated in light lines of Fig. 1(a-c). The inverse slope of the valley gives the value of C_s , which is labeled in red. The incompressible states with different C_s values locate at different densities $\langle n \rangle = 2 + C_s(\phi_{\text{TRI}}/\phi_0)$, at a finite TRI flux. From this one-to-one correspondence, it is sufficient to choose a certain flux (e.g., $\phi_{\text{TRI}}/\phi_0 = 1/36$, as shown by the dotted line in Fig. 1(a-c)) to determine the C_s from the density of the incompressible state. We set $t' = 0.1$, resulting in a QSH insulator for $\lambda_v < \lambda_v^c \approx 0.52$. Fixing $\lambda_v = 0.3 < \lambda_v^c$ and turning on h , the system can exhibit three different phases (QSH, AFI, TriI) at different h as shown in the $\chi_{\text{TRI}}(\phi_{\text{TRI}}/\phi_0 = 1/36)$ in Fig. 1(d). At $\beta = 10$, the valleys locate at different densities associated with different C_s , labeled in red. Next we fix $h = 1$, starting from a TriI at $\lambda_v = 0$. Increasing λ_v past a threshold induces a AFI, with further increases returning the system back to trivial, as shown in Fig. 1(e). While these phases are clearly observed at $\beta = 10$, the correct features already emerge at $\beta = 5$. This example illustrates the emergence of the intermediate AFI found in previous mean-field studies[18, 19] on the KMH model with sublattice potential at large U where the effective h is provided by U .

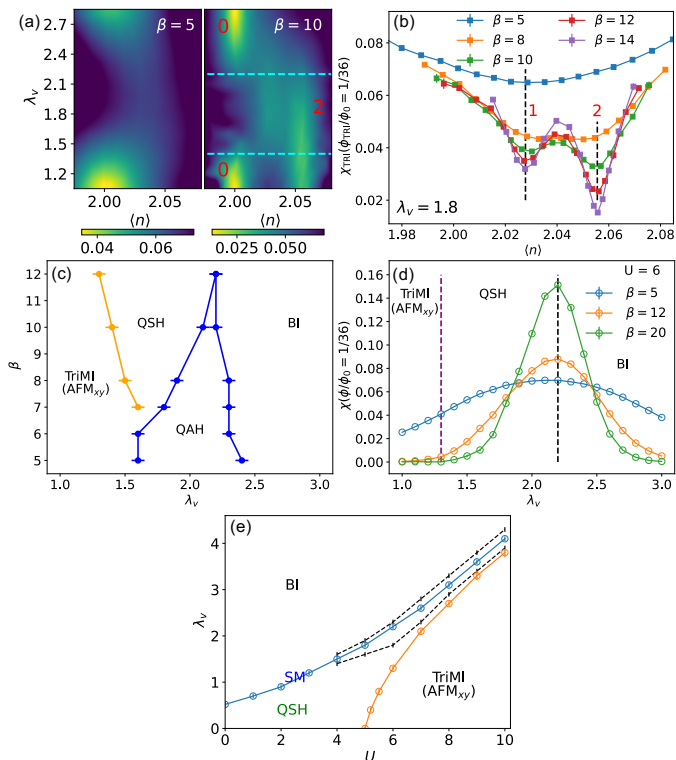


FIG. 2: Panel (a) shows $\chi_{\text{TRI}}(\phi_{\text{TRI}}/\phi_0 = 1/36)$ as a function of $\langle n \rangle$ and λ_v with $U = 6$ at $\beta = 5$ and 10 . The dashed lines label where the topological phase transitions happen. Panel (b) presents the same quantity fixing $\lambda_v = 1.8$ and varying temperatures. Panel (c) shows how the topology evolve as β and λ_v changes. Panel (d) shows the normal compressibility χ at the normal minimal flux ($\phi/\phi_0 = 1/36$). Panel (e) shows the $\lambda_v - U$ phase diagram at the lowest temperatures (see supplement). The other parameters for all panels are $t' = 0.1$. All results are from the DQMC simulations on a $6 \times 6 \times 2$ cluster.

To examine this picture, we next solve the KMH model

$$H_{\text{KM}} = H_{\text{KM}} + U \sum_{\mathbf{i}} \left(n_{\mathbf{i}\uparrow} - \frac{1}{2} \right) \left(n_{\mathbf{i}\downarrow} - \frac{1}{2} \right), \quad (3)$$

using the numerically exact DQMC method [21–24] mostly in a $6 \times 6 \times 2$ cluster due to the sign problem. The Jackknife estimate is used to calculate the error bar. We also compute bigger system size to gauge the finite-size effects (FSE) and demonstrate how the minimal magnetic field (ϕ (or $\phi_{\text{TRI}})/\phi_0 = 1/N_c = 1/36$) can minimize the FSE while approaching the zero-field topology.

We continue with $t' = 0.1$, consistent with the previous solvable example in Fig. 1, which exhibits a significant QSH gap $\Delta_{\text{QSH}} = 2\lambda_v^c \approx 1.04$ when $\lambda_v = U = 0$. As U increases, the half-filled system transitions into a TriMI with AFM $_{xy}$ at $U_c = 5$. Now considering a TriMI at fixed $U = 6$, we turn on λ_v . As indicated by χ_{TRI} in Fig. 2(a) at $\beta = 5$, the system remains trivial for small λ_v , appears to reach $C_s = 1$ in an intermediate region of λ_v , and becomes a BI for sufficiently large λ_v . This behavior is similar to that shown in Fig. 1(e) at

$\beta = 5$. From this analogy, one may infer that the intermediate region in Fig. 2(a) indicates the QAH phase corresponding to AFCI, consistent with the previous mean-field studies [18, 19]. However, this conclusion does not hold as we explore lower temperature $\beta = 10$ in Fig. 2(a). Surprisingly, the leading dip in the intermediate region shifts to $\langle n \rangle = 2.056$ ($C_s = 2$), indicating that the QAH feature transforms into an incipient QSH at low enough temperature. Fixing $\lambda_v = 1.8$, we examine the temperature evolution of χ_{TRI} in Fig. 2(b). At $\beta = 5$, the dip is located at $\langle n \rangle = 2.028$ (indicating $C_s = 1$). However, as β increases to 8, a second dip at $\langle n \rangle = 2.056$ (indicating $C_s = 2$) emerges, and with further increasing β , this dip dominates and hence stabilizes an incipient QSH insulator. The overall phase evolution as λ_v and β vary at $U = 6$ is depicted in Fig. 2(c). Note that the blue line shows the crossover from QAH to QSH or BI. At low temperature, the non-trivial topology that persists is the QSH effect.

The transitions from the intermediate QSH phase to the TriMI and BI are also intriguing. In Fig. 1(e), the valleys for different phases vanish abruptly at the phase boundary, indicating the topological phase transition (TPT) occurs through closing and reopening the single-particle gap. In contrast, the strongly correlated case at $\beta = 10$, shown in Fig. 2(a), exhibits distinctly different behaviors. At the upper phase boundary, the valleys already become increasingly indistinct before the TPT takes place. This is also evident in the compressibility under the normal minimal flux ($\phi/\phi_0 = 1/36$) at varying temperatures, as plotted in Fig. 2(d). We observed an extended quasi-semi-metallic region around the TPT at $\lambda_v = 2.2$ where the compressibility increases as temperature decreases indicating an extremely small gap. At the lower phase boundary of Fig. 2(a), the QSH valley persists beyond the TPT, while the TriMI valley dominates at small λ_v . This reveals that the charge gap does not close during the TPT. Consequently, in Fig. 2(d), the charge compressibility shows no evidence of this TPT, as indicated by the purple dashed line, similar to the previous studied gap-not-closing TPT driven by U at $\lambda_v = 0$ [24]. To summarize, we present the phase diagram in Fig. 2(e) based on DQMC results at the lowest temperature. The nontrivial topology persists as an incipient QSH effect when both U and λ_v are large, following $U \sim 2\lambda_v$. Although a large U or λ_v can destroy topology, these effects compete with each other. When both terms are strong, they tend to weaken each other's impact, allowing the QSH phase induced by SOC to remain. Increasing λ_v transitions the QSH phase into a BI, as indicated by the blue line in Fig. 2(e). Around this transition, an extended quasi-semimetallic region is observed, enclosed by the dashed lines in Fig. 2(e). Increasing U transitions the QSH into a TriMI without closing the charge gap, as depicted by the orange line.

We have shown that an incipient QSH rather than an AFCI persists when both U and λ_v are large and satisfies $U \sim 2\lambda_v$, as observed from the TRI compressibility. Next, we examine the antiferromagnetic spin correlations to assess the easy z -axis claim from mean-field studies [18, 19]. To ensure the system reaches the possible easy-axis region, we set

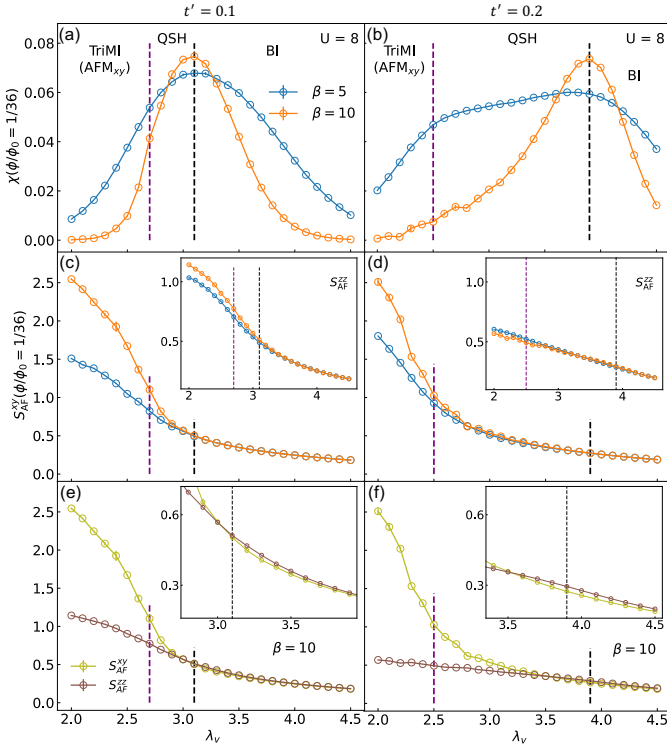


FIG. 3: The left and right columns present the normal compressibility and AF spin correlation at minimal flux as a function of λ_v for $t' = 0.1$ and $t' = 0.2$, respectively, at different temperatures ($\beta = 5, 10$) and $U = 8$. The compressibility is shown in panels (a) and (b). S_{AF}^{xy} is shown in panels (c) and (d), with S_{AF}^{zz} in the inset. Panels (a-d) share the same legend. Panels (e) and (f) compare S_{AF}^{xy} and S_{AF}^{zz} at $\beta = 10$. The dashed line depicts the TPT.

$U = 8$ and plot the normal charge compressibility, AFM_{xy} ($S_{\text{AF}}^{xy} = (1/N) \sum_{i,j} (-1)^{i+j} \langle (S_i^x S_j^x + S_i^y S_j^y) / 2 \rangle$) and AFM_z ($S_{\text{AF}}^{zz} = (1/N) \sum_{i,j} (-1)^{i+j} \langle S_i^z S_j^z \rangle$) spin correlations at minimal flux as a function of λ_v with different temperatures, as shown in Fig. 3. The first column (Fig. 3(a,c,e)) uses $t' = 0.1$, consistent with Fig. 2. Fig. 3(a) is qualitatively similar to Fig. 2(d) but shows a narrower QSH region due to stronger correlations. S_{AF}^{xy} increases along with β as the system reaches the TriMI phase while S_{AF}^{zz} remains almost independent of temperature in the intermediate topological region, as shown in Fig. 3(c). Fig. 3(e) provides a direct comparison between S_{AF}^{xy} and S_{AF}^{zz} at the lower temperature ($\beta = 10$), clearly showing that S_{AF}^{xy} dominates for small value of λ_v . S_{AF}^{zz} only slightly exceeds S_{AF}^{xy} in the quasi semi-metallic and BI region, where it does not grow with β . Thus, the claim of an easy-axis in the intermediate region is not supported. The second column (Fig. 3(b,d,f)) uses $t' = 0.2$, consistent with Ref. [18], with a larger QSH gap $\Delta_{\text{QSH}} = 2$ when $U = \lambda_v = 0$. As expected, a wider QSH region is observed in Fig. 3(b) compared to Fig. 3(a). The S_{AF}^{xy} is not significantly different between Fig. 3(c) and (d), while S_{AF}^{zz} is suppressed in the $t' = 0.2$ case. This aligns with the strong coupling analysis[25], where t' and U tend to flip the sign of spin between second neighbors frus-

trating the AFM_z . In Fig. 3(f), $S_{\text{AF}}^{xy} > S_{\text{AF}}^{zz}$ for most region, except for $\lambda_v > 3.6$, $S_{\text{AF}}^{zz} \approx S_{\text{AF}}^{xy}$ with little temperature dependence. The situation of $t' = 0.3, \psi = -\pi/3$ relevant to twisted MoTe_2 [19] is similar to that of the $t' = 0.2$ case (see supplement) since they share the same original QSH gap. The easy axis is not observed even in the $t' = 0.1$ case with a smaller QSH gap and stronger S_{AF}^{zz} , let alone in the other two cases.

We can also gain some insight on why QSH persists instead of AFCI from the normal compressibility as a function of density $\langle n \rangle$ and magnetic flux ϕ/ϕ_0 for the non-interacting AFCI, (Fig. 4(a)), and all three interacting cases discussed above (Fig. 4(b-d)) at $U = 8$. The signature of QSH effect is a short vertical valley at low field indicating the charge Chern number $C = 0$ and two bifurcating zero Landau levels (LLs) at high field referring to the $C = \pm 1$ incompressible states when the system breaks inversion symmetry $\lambda_v \neq 0$ (see supplement), as observed in experiments[4, 26]. In contrast, the QAH effect in AFCI contains only one of these LLs, as shown in Fig. 4(a). The QAH gap is around 0.24 and the valley is well resolved at $\beta = 5$. Here, the interplay between h and λ_v turns QSH into QAH. On the other hand, the QSH pattern persists in Fig. 4(b-d) for all interacting cases. The absence of long-range dominant AFM_z correlation at finite temperature allows both LLs to persist. Interestingly, the particle-hole symmetry-breaking case simulating twisted MoTe_2 in Fig. 4(d) shows the most robust QSH with highest critical field. That said, the AF fluctuation driven by interaction indeed suppresses the QSH gap and hence the critical field decreases significantly, particularly in Fig. 4(b) for $t' = 0.1$, with similar but less suppression is expected for the other two parameter sets. One might question whether DQMC can in principle host an emergent AFCI state at all in the presence of strong correlations. This is indeed the case, as confirmed in the Haldane-Hubbard model (see supplement), consistent with earlier studies[27–30]. Therefore, in the KMH model with sub-lattice potential, there is no AFCI state for large λ_v and U driven by easy-axis AFM_z , but rather an incipient QSH state.

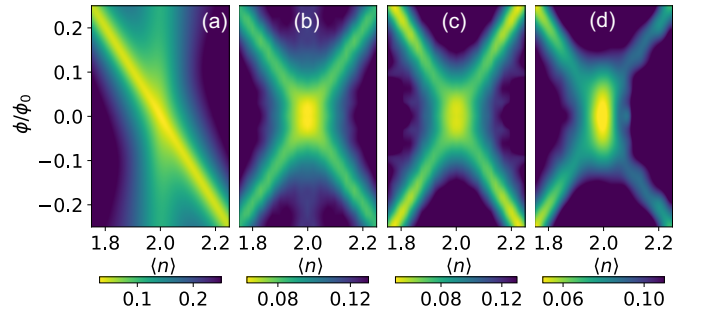


FIG. 4: The compressibility as a function of density and magnetic flux for the non-interacting case (a) $t' = 0.1, h = 1, \lambda_v = 0.6$ and interacting cases: (b) $t' = 0.1, U = 8, \lambda_v = 2.9$, (c) $t' = 0.2, U = 8, \lambda_v = 3.2$, and (d) $t' = 0.3, \psi = -\pi/3, U = 8, \lambda_v = 3.2$. The inverse temperature is $\beta = 5$ for all panels.

CONCLUDING REMARKS

We have employed DQMC into studying the KMH model across several parameter sets. Our findings indicate that, under strong correlations, the system generally maintains a QSH state within a narrow range of sublattice potential λ_v , albeit with a small gap. As λ_v increases, the QSH state transitions into a band insulator (BI) by closing and reopening the charge gap. The wide compressible region around the transition leads to an extended semi-metallic region. When λ_v decreases, the QSH state transitions into a TriMI with AFM_{xy} without closing the charge gap. The QAH feature is only observed at high temperature and crossovers to an incipient QSH state when the topological gap stabilizes, due to the absence of long-range AFM_z correlations at finite temperature. Our study is consistent with the experimental observation that in twisted bilayer MoTe₂[1–3] and WSe₂[4] as well as AB stacked MoTe₂/WSe₂[5, 6], where QSH is consistently observed at even-integer filling over a wide range of parameters.

Acknowledgements We thank Xiao Di and Xiaodong Xu for insightful discussions, Cristian Batista for suggesting the pedagogical example of applying an AFM_z Zeeman field. This work was supported by the Center for Quantum Sensing and Quantum Materials, a DOE Energy Frontier Research Center, grant DE-SC0021238 (P. M. and P. W. P.). PWP also acknowledges NSF DMR-2111379 for partial funding of the work on QSH in the KM model.

-
- [1] H. Park, J. Cai, E. Anderson, Y. Zhang, J. Zhu, X. Liu, C. Wang, W. Holtzmann, C. Hu, Z. Liu, et al., *Nature* **622**, 74 (2023).
- [2] J. Cai, E. Anderson, C. Wang, X. Zhang, X. Liu, W. Holtzmann, Y. Zhang, F. Fan, T. Taniguchi, K. Watanabe, et al., *Nature* (2023).
- [3] Y. Zeng, Z. Xia, K. Kang, J. Zhu, P. Knüppel, C. Vaswani, K. Watanabe, T. Taniguchi, K. F. Mak, and J. Shan, *Nature* **622**, 69 (2023).
- [4] B. A. Foutty, C. R. Kometter, T. Devakul, A. P. Reddy, K. Watanabe, T. Taniguchi, L. Fu, and B. E. Feldman, *Science* **384**, 343 (2024), <https://www.science.org/doi/pdf/10.1126/science.adi4728>, URL <https://www.science.org/doi/abs/10.1126/science.adi4728>.
- [5] T. Li, S. Jiang, B. Shen, Y. Zhang, L. Li, Z. Tao, T. Devakul, K. Watanabe, T. Taniguchi, L. Fu, et al., *Nature* **600**, 641 (2021).
- [6] Z. Tao, B. Shen, S. Jiang, T. Li, L. Li, L. Ma, W. Zhao, J. Hu, K. Pistunova, K. Watanabe, et al., *Phys. Rev. X* **14**, 011004 (2024), URL <https://link.aps.org/doi/10.1103/PhysRevX.14.011004>.
- [7] F. Xu, Z. Sun, T. Jia, C. Liu, C. Xu, C. Li, Y. Gu, K. Watanabe, T. Taniguchi, B. Tong, et al., *Phys. Rev. X* **13**, 031037 (2023), URL <https://link.aps.org/doi/10.1103/PhysRevX.13.031037>.
- [8] Z. Lu, T. Han, Y. Yao, A. P. Reddy, J. Yang, J. Seo, K. Watanabe, T. Taniguchi, L. Fu, and L. Ju, *Nature* **626**, 759 (2024).
- [9] R. L. Willett, *Reports on Progress in Physics* **76**, 076501 (2013), URL <https://dx.doi.org/10.1088/0034-4885/76/7/076501>.
- [10] C. Nayak, S. H. Simon, A. Stern, M. Freedman, and S. Das Sarma, *Rev. Mod. Phys.* **80**, 1083 (2008), URL <https://link.aps.org/doi/10.1103/RevModPhys.80.1083>.
- [11] K. Kang, B. Shen, Y. Qiu, Y. Zeng, Z. Xia, K. Watanabe, T. Taniguchi, J. Shan, and K. F. Mak, *Nature* **628**, 522 (2024).
- [12] H. Park, J. Cai, E. Anderson, X.-W. Zhang, X. Liu, W. Holtzmann, W. Li, C. Wang, C. Hu, Y. Zhao, et al., arXiv e-prints arXiv:2406.09591 (2024), 2406.09591.
- [13] F. Wu, T. Lovorn, E. Tutuc, I. Martin, and A. H. MacDonald, *Phys. Rev. Lett.* **122**, 086402 (2019), URL <https://link.aps.org/doi/10.1103/PhysRevLett.122.086402>.
- [14] M. Hohenadler, T. C. Lang, and F. F. Assaad, *Phys. Rev. Lett.* **106**, 100403 (2011), URL <https://link.aps.org/doi/10.1103/PhysRevLett.106.100403>.
- [15] M. Hohenadler, Z. Y. Meng, T. C. Lang, S. Wessel, A. Muramatsu, and F. F. Assaad, *Phys. Rev. B* **85**, 115132 (2012), URL <https://link.aps.org/doi/10.1103/PhysRevB.85.115132>.
- [16] S. Rachel and K. Le Hur, *Phys. Rev. B* **82**, 075106 (2010), URL <https://link.aps.org/doi/10.1103/PhysRevB.82.075106>.
- [17] D. Lessnich, C. Gauvin-Ndiaye, R. Valentí, and A.-M. S. Tremblay, *Phys. Rev. B* **109**, 075143 (2024), URL <https://link.aps.org/doi/10.1103/PhysRevB.109.075143>.
- [18] K. Jiang, S. Zhou, X. Dai, and Z. Wang, *Phys. Rev. Lett.* **120**, 157205 (2018), URL <https://link.aps.org/doi/10.1103/PhysRevLett.120.157205>.
- [19] X. Liu, Y. He, C. Wang, X.-W. Zhang, T. Cao, and D. Xiao, *Phys. Rev. Lett.* **132**, 146401 (2024), URL <https://link.aps.org/doi/10.1103/PhysRevLett.132.146401>.
- [20] F. D. M. Haldane, *Phys. Rev. Lett.* **61**, 2015 (1988), URL <https://link.aps.org/doi/10.1103/PhysRevLett.61.2015>.
- [21] P. Mai, B. E. Feldman, and P. W. Phillips, *Phys. Rev. Res.* **5**, 013162 (2023), URL <https://link.aps.org/doi/10.1103/PhysRevResearch.5.013162>.
- [22] P. Mai, J. Zhao, B. E. Feldman, and P. W. Phillips, *Nature Communications* **14**, 5999 (2023).
- [23] P. Mai, E. W. Huang, J. Yu, B. E. Feldman, and P. W. Phillips, *npj Quantum Materials* **8**, 14 (2023).
- [24] P. Mai, J. Zhao, T. A. Maier, B. Bradlyn, and P. W. Phillips, *Phys. Rev. B* **110**, 075105 (2024), URL <https://link.aps.org/doi/10.1103/PhysRevB.110.075105>.
- [25] S. Rachel and K. Le Hur, *Phys. Rev. B* **82**, 075106 (2010), URL <https://link.aps.org/doi/10.1103/PhysRevB.82.075106>.
- [26] M. König, S. Wiedmann, C. Brüne, A. Roth, H. Buhmann, L. W. Molenkamp, X.-L. Qi, and S.-C. Zhang, *Science* **318**, 766 (2007), <https://www.science.org/doi/pdf/10.1126/science.1148047>, URL <https://www.science.org/doi/abs/10.1126/science.1148047>.
- [27] T. I. Vanhala, T. Siro, L. Liang, M. Troyer, A. Harju, and P. Törmä, *Phys. Rev. Lett.* **116**, 225305 (2016), URL <https://link.aps.org/doi/10.1103/PhysRevLett.116.225305>.
- [28] C. Shao, E. V. Castro, S. Hu, and R. Mondaini, *Phys. Rev.*

- B 103**, 035125 (2021), URL <https://link.aps.org/doi/10.1103/PhysRevB.103.035125>.
- [29] J. Imriška, L. Wang, and M. Troyer, *Phys. Rev. B* **94**, 035109 (2016), URL <https://link.aps.org/doi/10.1103/PhysRevB.94.035109>.
- [30] T. Mertz, K. Zantout, and R. Valentí, *Phys. Rev. B* **100**, 125111 (2019), URL <https://link.aps.org/doi/10.1103/PhysRevB.100.125111>.

Incipient quantum spin Hall insulator in Kane-Mele-Hubbard model: supplemental material

Peizhi Mai¹, Jinchao Zhao¹, Philip W. Phillips^{1,†}

¹Department of Physics and Institute of Condensed Matter Theory,
University of Illinois at Urbana-Champaign, Urbana, IL 61801, USA

(Dated: today)

FINITE-SIZE EFFECTS MINIMIZED BY MAGNETIC FLUX

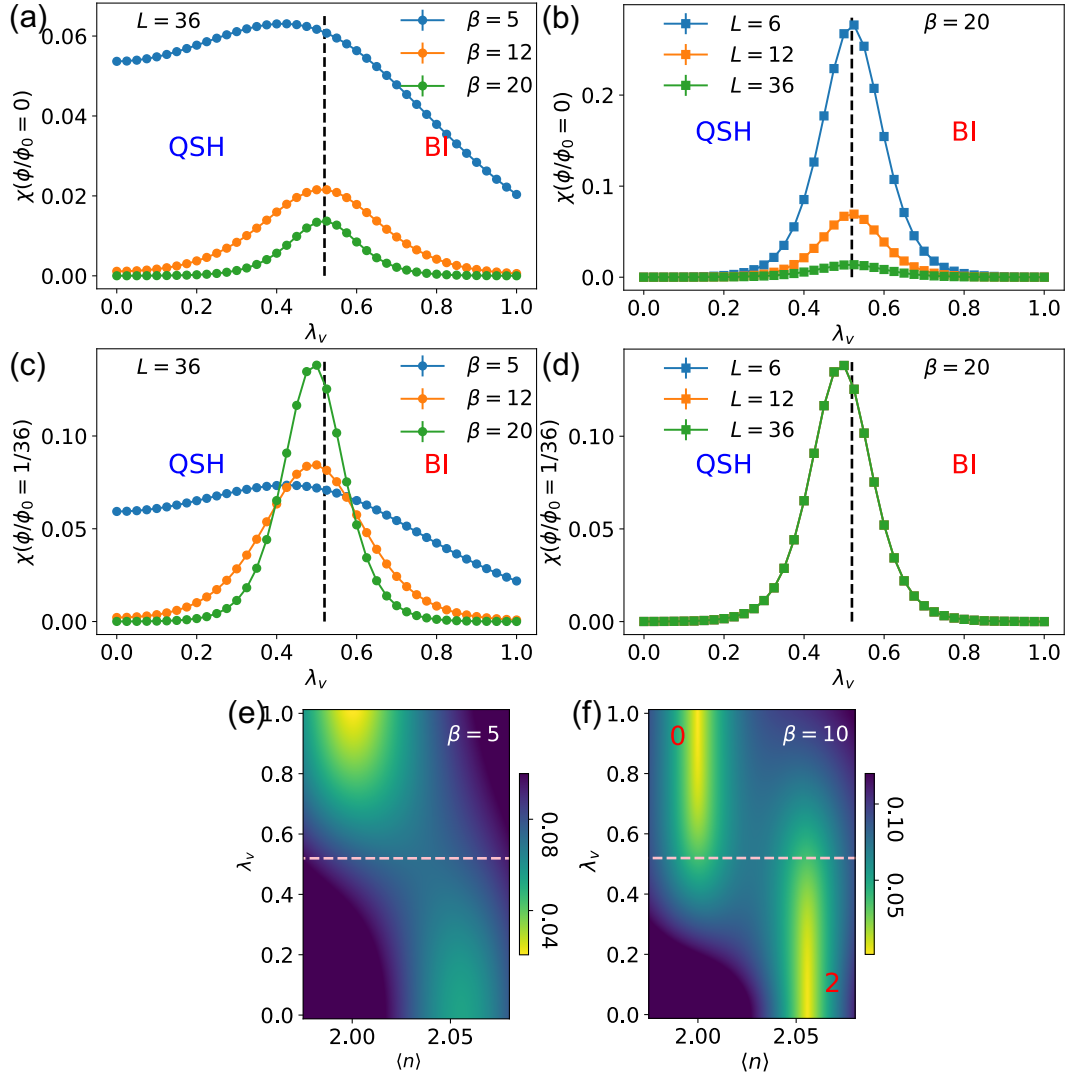


FIG. S1: (First row) Non-interacting compressibility at zero flux as a function of sublattice potential difference λ_v (a) with varying temperature at $L = 36$ and (b) with varying cluster size at $\beta = 20$. (Second row) Non-interacting compressibility at magnetic flux ($\phi/\phi_0 = 1/36$) as a function of sublattice potential difference λ_v (c) with varying temperature at $L = 36$ and (d) with varying cluster size at $\beta = 20$. Panels (e) and (f) show the TRI Compressibility χ_{TRI} at TRI flux $\phi_{\text{TRI}}/\phi_0 = 1/36$ as a function of $\langle n \rangle$ and λ_v with $\beta = 5$ and 10 respectively. The dashed line depicts the transition. All panels share the parameter set $t' = 0.1, \psi = -\pi/2, h = 0$.

In this section, we consider three topological phase transitions (TPT) mentioned in the main text and show how the finite-size effects can be minimized by turning on a minimal normal or time-reversal-invariant (TRI) magnetic flux. For all these non-interacting example, we employ the flux $\phi/\phi_0 = 1/36 = 0.028$ or $\phi_{\text{TRI}}/\phi_0 = 1/36 = 0.028$, so that the conclusion applies to the interacting systems where we conduct the determinant quantum Monte-carlo (DQMC) simulations on a $L = 6$ cluster (the

cluster size is $N_{\text{site}} = L \times L \times 2$).

In the first example, we look into the Kane-Mele model with a sub-lattice potential λ_v :

$$H_{\text{KM}} = t \sum_{\langle ij \rangle \sigma} e^{i\phi_{i,j}} c_{i\sigma}^\dagger c_{j\sigma} + t' \sum_{\langle\langle ij \rangle\rangle \sigma} e^{\pm i\psi\sigma} e^{i\phi_{i,j}} c_{i\sigma}^\dagger c_{j\sigma} - \mu \sum_{i,\sigma} n_{i\sigma} + \lambda_v \left(\sum_{i \in A, \sigma} n_{i\sigma} - \sum_{i \in B, \sigma} n_{i\sigma} \right), \quad (\text{S1})$$

We fix $t' = 0.1$, $\psi = -\pi/2$ and vary λ_v . The system is a quantum spin Hall (QSH) insulator for $\lambda_v < 3\sqrt{3}t' = 0.52$ and a trivial band insulator (BI) for $\lambda_v > 3\sqrt{3}t' = 0.52$. The single particle charge gap closes at the transition point $\lambda_{vc} = 0.52$. We first compute the compressibility without an external magnetic field. The result is shown in Fig. S1(a) at varying temperatures $\beta = 5, 12, 20$ for a $L = 36$ cluster (assumed to be large enough). The compressibility for all λ_v decreases with temperature. The charge gap closes at the TPT, as signalled by the peak of compressibility. Next we gauge the finite-size effect by varying L at the lowest temperature $\beta = 20$, as shown in Fig. S1(b). The finite-size effect grows as the system approach the phase transition from either side, rendering the results from smaller cluster size unreliable. We then look at the same temperature and cluster size variation respectively in Fig. S1(c) and (d) with a minimal magnetic flux $\phi/\phi_0 = 1/36$. Comparing Fig. S1(a) and (c), we find that in the presence of the small flux, the compressibility near the transition instead grows with temperature, making the peak more pronounced and thereby facilitating the detection of the transition. That indicates the magnetic flux turns the semi-metal into a metal. We also observe that the location of the peak slightly deviates from the transition by $\Delta\lambda_v = 0.025 \approx \phi/\phi_0$ as a side effect of the magnetic flux. This is acceptable as in the interacting case the λ_v interval is 0.1. Remarkably, in Fig. S1(d), all the curves for different system size collapse at the lowest temperature, in contrast to Fig. S1(b). There is no visible finite size effect even though we conduct the simulation on the $L = 6$. Similar situation also applies to the TRI magnetic flux. Thus, we fix the TRI flux at $\phi_{\text{TRI}}/\phi_0 = 1/36$ and plot the TRI compressibility as a function density and λ_v at $\beta = 5$ and 10 to observe the phase evolution.

Similar behavior is observed in the TPTs when fixing $\lambda_v = 0.3$ and increasing the zz -antiferromagnetic (AFM_z) Zeeman field h , as shown in Fig. S2, and when fixing $h = 1$ and increasing λ_v , as shown in Fig. S3. To summarize, employing a small magnetic flux minimizes the finite-size effect and makes the charge-gap-closing transition more pronounced, though it introduces a small deviation on the estimate of the transition point.

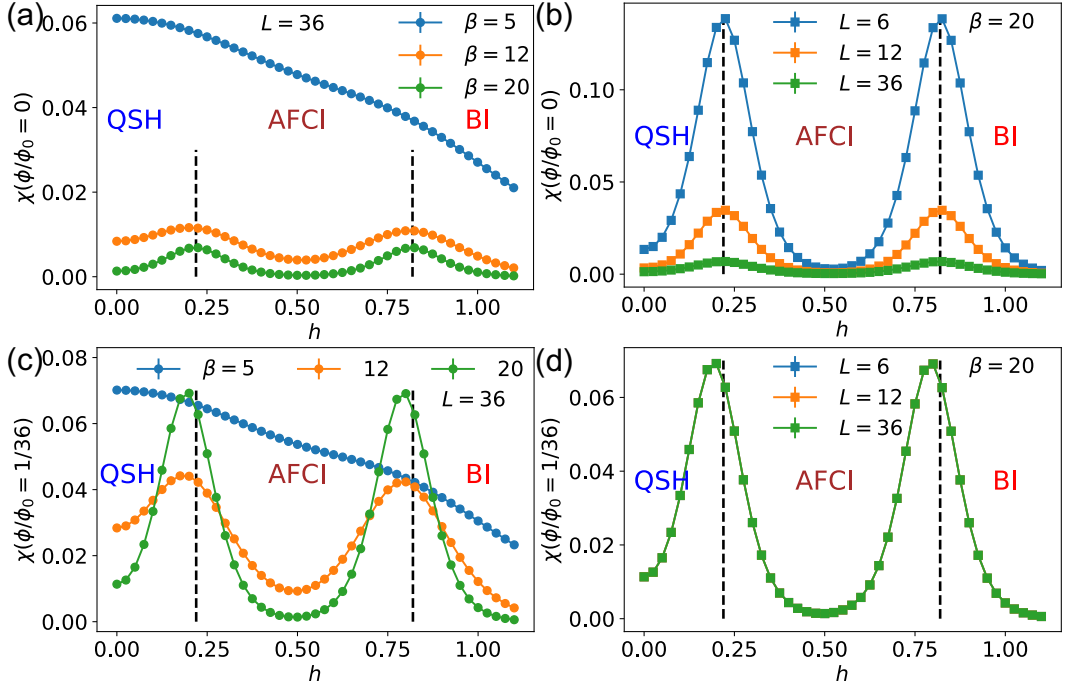


FIG. S2: (First row) Non-interacting compressibility at zero flux as a function of AFM_z Zeeman field h (a) with varying temperature at $L = 36$ and (b) with varying cluster size at $\beta = 20$. (Second row) Non-interacting compressibility at magnetic flux ($\phi/\phi_0 = 1/36$) as a function of AFM_z Zeeman field h (c) with varying temperature at $L = 36$ and (d) with varying cluster size at $\beta = 20$. All panels share the parameter set $t' = 0.1$, $\psi = -\pi/2$, $\lambda_v = 0.3$.

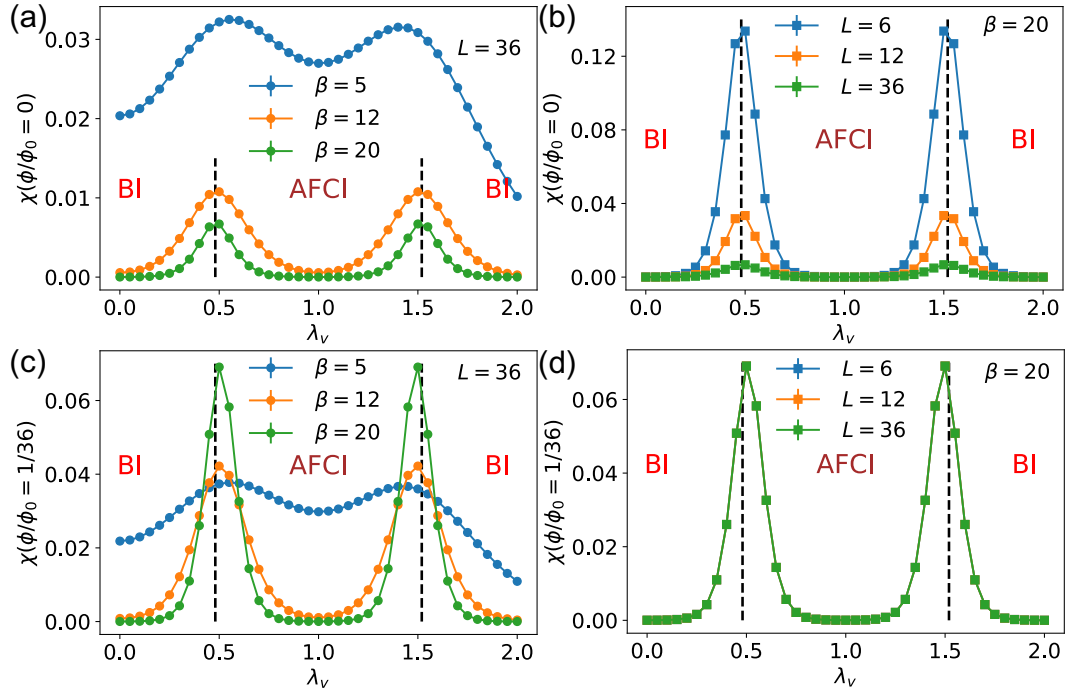


FIG. S3: (First row) Non-interacting compressibility at zero flux as a function of sublattice potential difference λ_v (a) with varying temperature at $L = 36$ and (b) with varying cluster size at $\beta = 20$. (Second row) Non-interacting compressibility at magnetic flux ($\phi/\phi_0 = 1/36$) as a function of sublattice potential difference λ_v (c) with varying temperature at $L = 36$ and (d) with varying cluster size at $\beta = 20$. All panels share the parameter set $t' = 0.1, \psi = -\pi/2, h = 1$.

LANDAU LEVEL FEATURE FOR QSH EFFECTS

In this section, we discuss the Landau level signature for the QSH effects. In this discussion we consider the KM model with $t' = 0.2, \psi = -\pi/2$. We first set $\lambda_v = 0$ and plot the compressibility as a function of magnetic flux and density in Fig. S4(a). There is one sharp vertical valley indicating a zero charge Chern number due to time-reversal symmetry. Taking a cut at $\phi/\phi_0 = 0.07$ and 0.28 , we plot the density ($\langle n \rangle, \langle n_\uparrow \rangle, \langle n_\downarrow \rangle$) vs μ relations in Fig. S4(b) and (c) respectively. For small flux $\phi/\phi_0 = 0.07$, the opposite spins carry opposite Chern number and are in incompressible states within an overlapped region of μ , making the combined system a spin Chern insulator. For the high flux $\phi/\phi_0 = 0.28$, there is no overlapped region of μ where opposite spins are incompressible, there by no valley is observed. Now let's look at the case with $\lambda_v = 0.5$, shown in the second row of Fig. S4. In Fig. S4(d), we observe in addition to the central valley for QSH, two bifurcate Landau levels (LLs) appear at high fluxes signalling the spins carrying opposite Chern number. Taking the cut at the higher flux (Fig. S4(f)), we find that while one spin is in a QAH state, the other spin is in a trivial state, thereby making the total system a QAH insulator and explaining the left and right moving LLs. In order to observe such the bifurcate LLs, we need to break the inversion symmetry with λ_v .

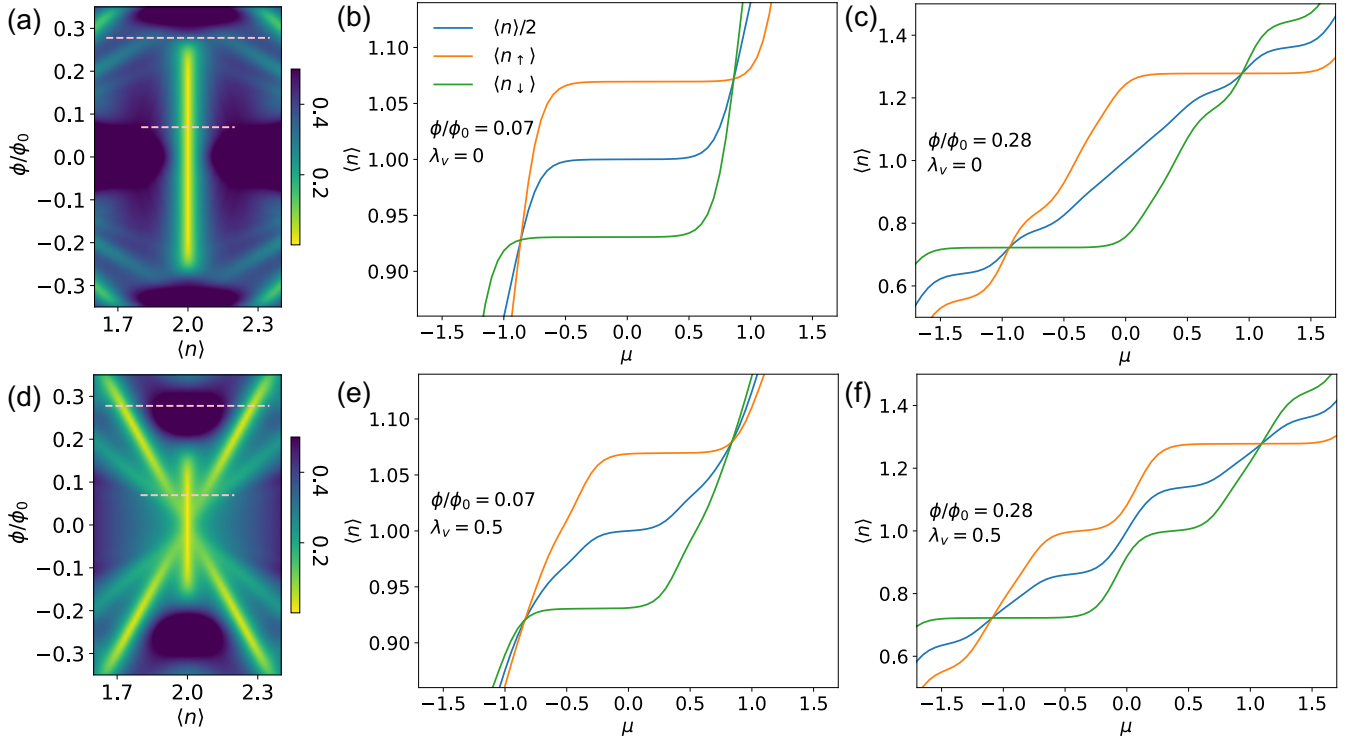


FIG. S4: Panels (a) and (d) show the compressibility as a function of $\langle n \rangle$ and magnetic flux ϕ at $\lambda_v = 0$ and 0.5 respectively. Panels (b) and (e) show $\langle n \rangle, \langle n_\uparrow \rangle, \langle n_\downarrow \rangle$ all as a function of μ at fixed $\phi/\phi_0 = 0.07$ for $\lambda_v = 0$ and 0.5 respectively. Panels (c) and (f) show the same quantity at fixed $\phi/\phi_0 = 0.28$.

SUPPLEMENTAL DATA FOR THE PHASE DIAGRAM AT $t' = 0.1, \psi = -\pi/2$

In this section, we provide the complete data set to determine the phase diagram in Fig. 2(e). First we show the compressibility at the minimal flux with varying temperature for all U in Fig. S5. The peak locates the semi-metallic TPT. We observe that as U increases, an extended quasi-semi-metallic region appears around this transition, in contrast to the sharp peak in Fig. S5a at $U = 0$. The trivial Mott insulator (TriMI) emerges for $U > 5$. To determine the charge-gap-not-closing TPT from QSH to TriMI, we compute the TRI compressibility as shown in Fig. S6 at the minimal flux and lowest temperature restricted by the sign problem. Based on the position of its leading dip, we estimate when the TPT takes place.

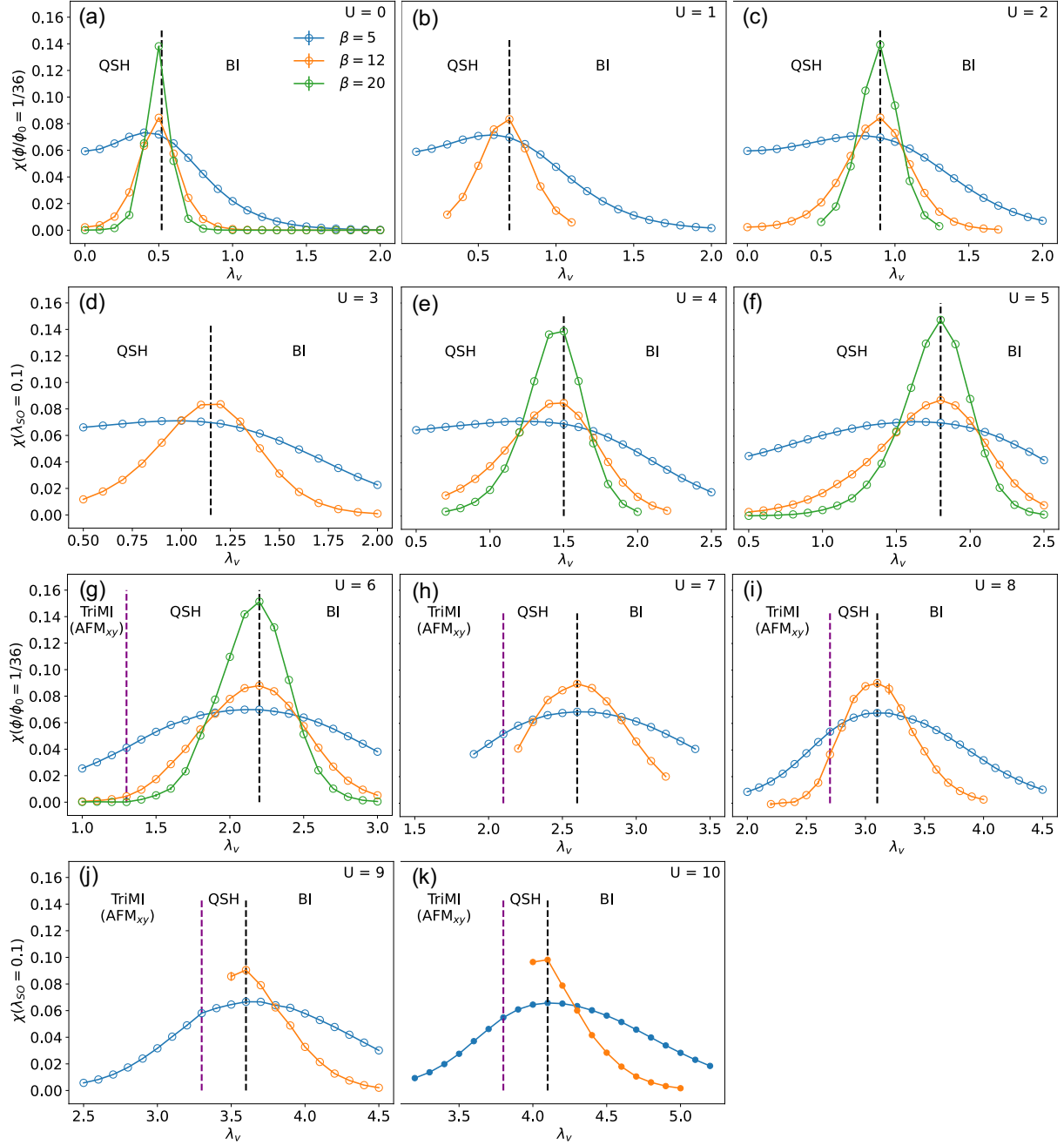


FIG. S5: Compressibility at the minimal flux as a function of sublattice potential difference λ_v under varying temperature for all U ranging from 0 to 10. All panels share the same legend and the parameter set $t' = 0.1, \psi = -\pi/2$.

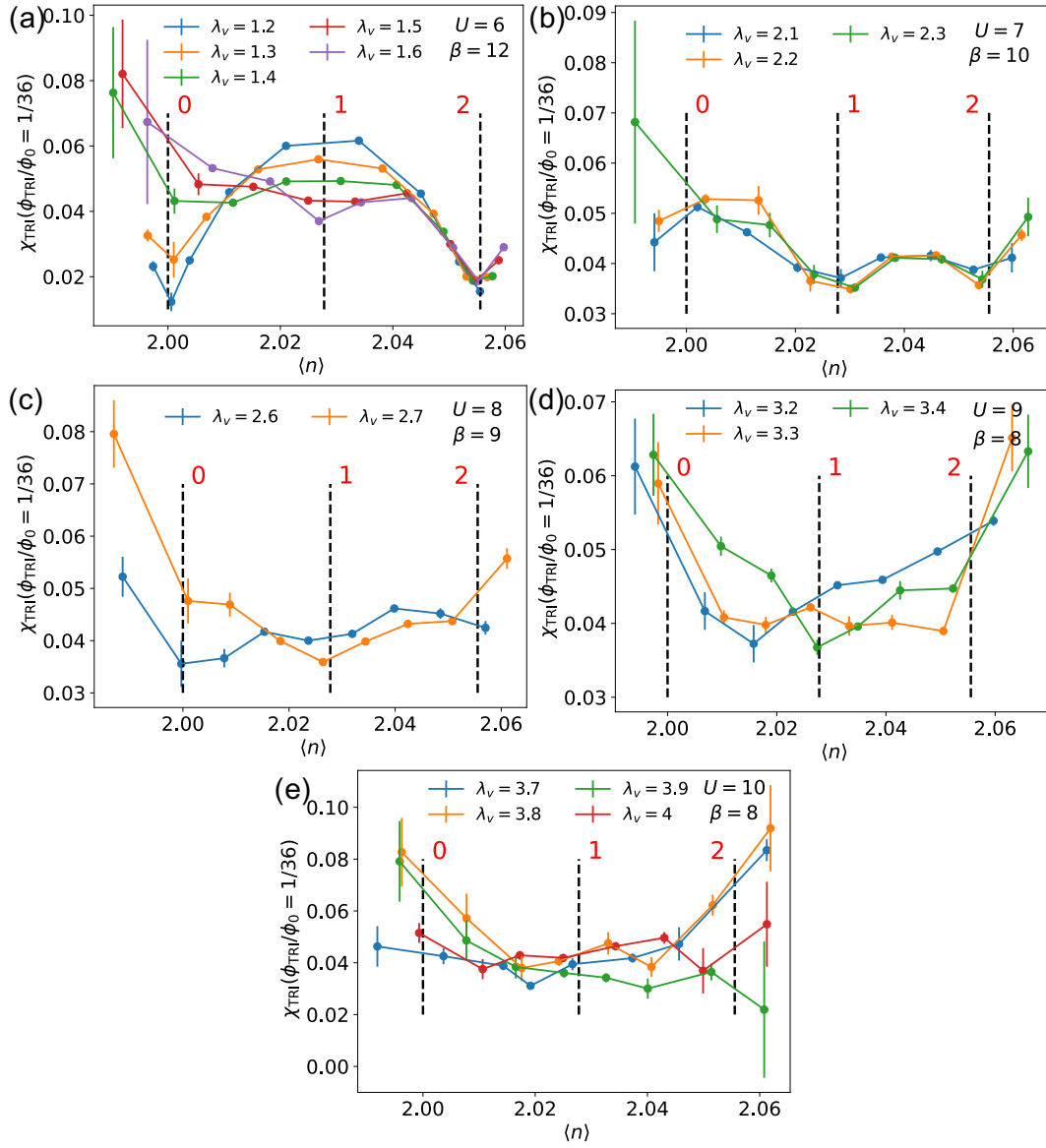


FIG. S6: TRI Compressibility at the minimal TRI flux as a function of density for varying λ_v at the lowest temperature for all U ranging from 6 to 10. All panels share the same parameter set $t' = 0.1, \psi = -\pi/2$.

COMPLETE DATA SET FOR COMPRESSIBILITY AND SPIN CORRELATIONS AT $U = 6$ AND 8

In this section, we compare the three Kane-Mele parameter sets: $t' = 0.1, \psi = \pi/2$ as focused in the main text, $t' = 0.2, \psi = \pi/2$ from [1] and $t' = 0.3, \psi = \pi/3$ from [2] relevant to twisted MoTe₂, in the presence of strong correlations $U = 6$ and 8.

We present comparison of compressibility and antiferromagnetic (AF) spin correlation among these three cases at $U = 6$ in Fig. S7. $U = 6$ is sufficiently strong to obtain a TriMI for $t' = 0.1, \psi = -\pi/2$ with a small λ_v , but not for the other two cases with a stronger original (when $U = \lambda_v = 0$) QSH gap. Accompanied with that, the S_{AF}^{xy} is weaker for $t' = 0.2, \psi = -\pi/2$ than $t' = 0.1, \psi = -\pi/2$, and further weakened for $t' = 0.3, \psi = -\pi/3$, as shown in Fig. S7(d-f). Also, S_{AF}^{xy} increases the most with decreasing T for $t' = 0.1, \psi = -\pi/2$, and less for $t' = 0.2, \psi = -\pi/2$. It is basically temperature-independent for $t' = 0.3, \psi = -\pi/3$, similar to S_{AF}^{zz} in all three cases. The comparison between S_{AF}^{xy} and S_{AF}^{zz} is given in Fig. S7(g-i). For most of the case, we only observe $S_{AF}^{xy} > S_{AF}^{zz}$, namely an easy-plane. Only in a small region around the TPT for $t' = 0.2, \psi = -\pi/2$ and $t' = 0.2, \psi = -\pi/2$, shown in the insets of Fig. S7(h) and (i) respectively, we find S_{AF}^{zz} slightly larger than S_{AF}^{xy} . However, as mentioned above, there is little temperature dependence in this region, and the difference is very tiny. Thus, we conclude that there is no easy-axis.

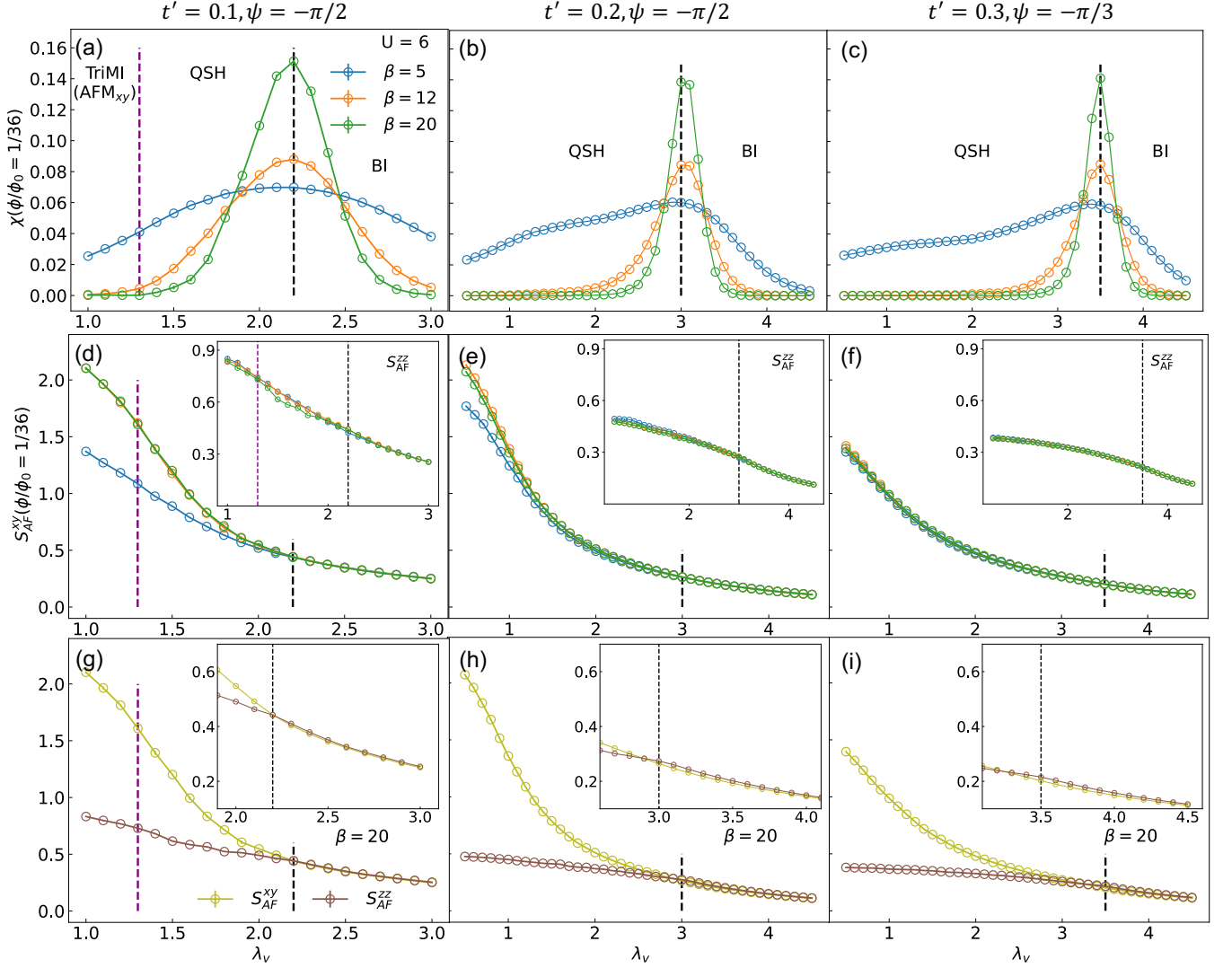


FIG. S7: Compressibility and antiferromagnetic (AF) spin correlations at the minimal flux as a function of sublattice potential difference λ_v under varying temperature ($\beta = 5$ and 12) for $t' = 0.1, \psi = -\pi/2$ (left column), $t' = 0.2, \psi = -\pi/2$ (middle column), and $t' = 0.3, \psi = -\pi/3$ (right column). The first row shows the compressibility. The second row shows S_{AF}^{xy} and S_{AF}^{zz} (inset) at different temperatures. The third row compares S_{AF}^{xy} and S_{AF}^{zz} at the lowest T ($\beta = 10$), with the inset zooming in the region around the semi-metallic transition. All panels share the same legend and are at $U = 6$.

The $U = 8$ case is shown in Fig. S8 including the $t' = 0.3, \psi = -\pi/3$, compared to Fig. 3 in the main text. Here the S_{AF}^{xy} becomes the strongest in $t' = 0.3, \psi = -\pi/3$ at $\beta = 5$. However, we can not reach lower temperature due to the sign problem. On the other hand, S_{AF}^{zz} is the most suppressed for $t' = 0.3, \psi = -\pi/3$. The comparison between S_{AF}^{xy} and S_{AF}^{zz} is similar to the $U = 6$ case. Hence, we again conclude that there is no easy axis.

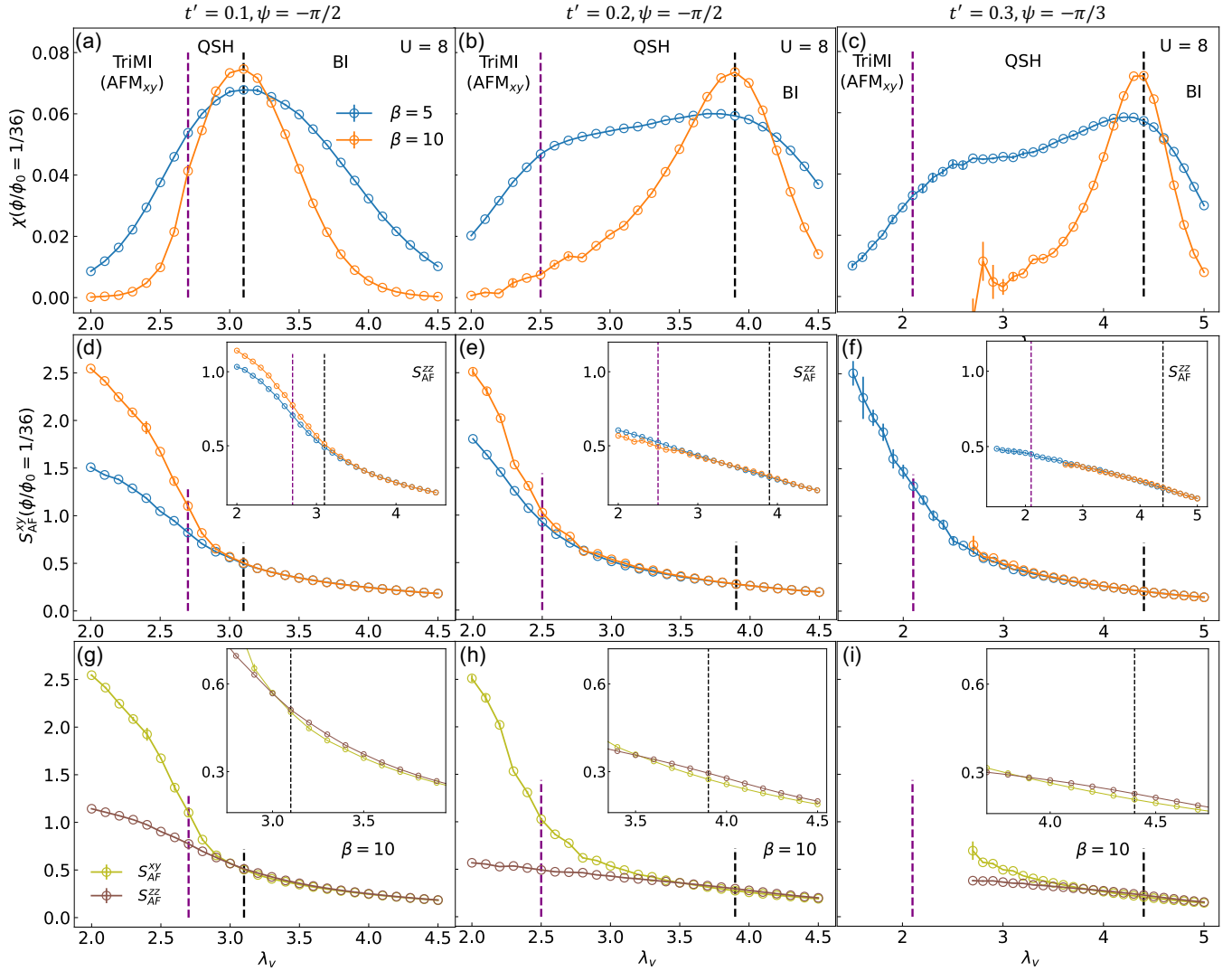


FIG. S8: Compressibility and AF spin correlations at the minimal flux as a function of sublattice potential difference λ_v under varying temperature ($\beta = 5$ and 12) for $t' = 0.1, \psi = -\pi/2$ (left column), $t' = 0.2, \psi = -\pi/2$ (middle column), and $t' = 0.3, \psi = -\pi/3$ (right column). The first row shows the compressibility. The second row shows S_{AF}^{xy} and S_{AF}^{zz} (inset) at different temperatures. The third row compares S_{AF}^{xy} and S_{AF}^{zz} at the lowest T ($\beta = 10$), with the inset zooming in the region around the semi-metallic transition. All panels share the same legend and are at $U = 8$.

ANTIFERROMAGNETIC CHERN INSULATOR IN THE HALDANE-HUBBARD MODEL

In this section, we explore a different model, the spinful Haldane-Hubbard model[3–6]. This model breaks time reversal symmetry explicitly. A quantum anomalous Hall effect obtains at $U = 0$ and half-filling with Chern number $C = 2$. For large U and λ_v , an antiferromagnetic Chern insulator (AFCI) obtains with $C = 1$, as confirmed by multiple methods[3–6]. Here we show that our method also supports such a state, in contrast to the Kane-Mele-Hubbard (KMH) case. We show the compressibility at the minimal flux under varying temperatures in Fig. S9(a). The double peak structure separates the intermediate topological phase from the trivial states on both sides by a gap-closing TPT. This model maintains $SU(2)$ symmetry. Therefore we only show S_{AF}^{zz} in Fig. S9(b) and it grows as temperature decreases. To determine the topology in the intermediate phase, we stick to the minimal flux and plot the compressibility as a function of density and λ_v in Fig. S9(c-e). As temperature reduces, the Chern number stabilizes to $C = 1$, consistent with the previous study. These results show our method can spot the AFCI state when it exists and hence support our conclusion that incipient QSH instead of AFCI persists in the KMH model when both U and λ_v are large.

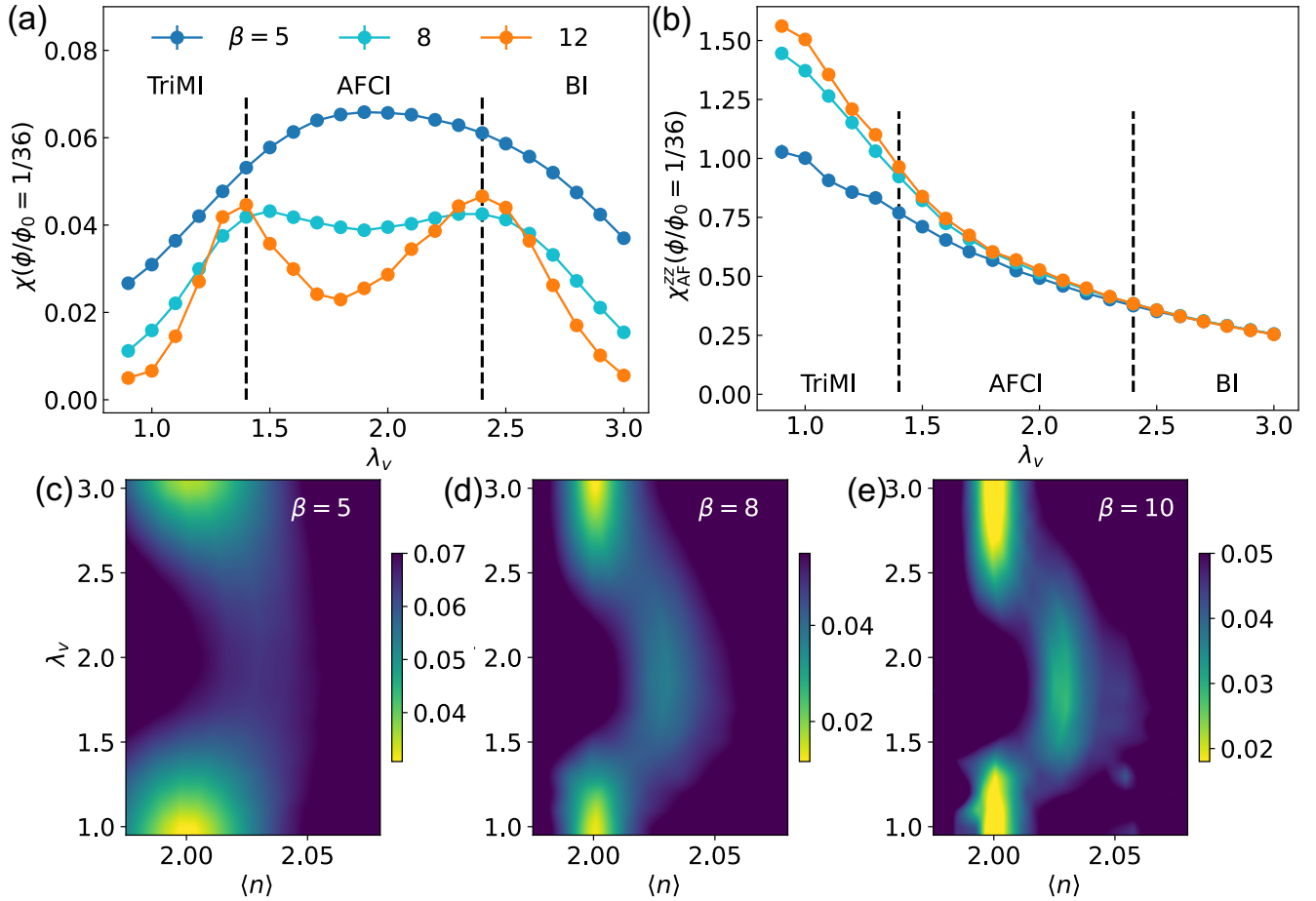


FIG. S9: Results from DQMC simulations on Haldane-Hubbard model at $t' = 0.1$, $\psi = -\pi/2$, $U = 6$. The first row shows the compressibility (a) and AF spin correlations (b) at the minimal flux as a function λ_v with fixed $\mu = 0$. The second row shows the compressibility at the minimal flux as a function λ_v and $\langle n \rangle$ at different temperatures.

- [1] K. Jiang, S. Zhou, X. Dai, and Z. Wang, Phys. Rev. Lett. **120**, 157205 (2018), URL <https://link.aps.org/doi/10.1103/PhysRevLett.120.157205>.
- [2] X. Liu, Y. He, C. Wang, X.-W. Zhang, T. Cao, and D. Xiao, Phys. Rev. Lett. **132**, 146401 (2024), URL <https://link.aps.org/doi/10.1103/PhysRevLett.132.146401>.

- [3] T. I. Vanhala, T. Siro, L. Liang, M. Troyer, A. Harju, and P. Törmä, Phys. Rev. Lett. **116**, 225305 (2016), URL <https://link.aps.org/doi/10.1103/PhysRevLett.116.225305>.
- [4] C. Shao, E. V. Castro, S. Hu, and R. Mondaini, Phys. Rev. B **103**, 035125 (2021), URL <https://link.aps.org/doi/10.1103/PhysRevB.103.035125>.
- [5] J. Imriška, L. Wang, and M. Troyer, Phys. Rev. B **94**, 035109 (2016), URL <https://link.aps.org/doi/10.1103/PhysRevB.94.035109>.
- [6] T. Mertz, K. Zantout, and R. Valentí, Phys. Rev. B **100**, 125111 (2019), URL <https://link.aps.org/doi/10.1103/PhysRevB.100.125111>.